Chemistry and Kinematics of Red Supergiant Stars in the Young Massive Cluster NGC 2100

L. R. Patrick[1]⋆, C. J. Evans[1,2], B. Davies[3], R-P. Kudritzki[4,5], N. Bastian[3], E. Lapenna[6], M

[1] *Institute for Astronomy, University of Edinburgh, Royal Observatory Edinburgh, Blackford Hill, Edinburgh EH9 3HJ, UK*
[2] *UK Astronomy Technology Centre, Royal Observatory Edinburgh, Blackford Hill, Edinburgh EH9 3HJ, UK*
[3] *Astrophysics Research Institute, Liverpool John Moores University, Liverpool Science Park ic2, 146 Brownlow Hill, Liverpool L3 5RF, UK*
[4] *Institute for Astronomy, University of Hawaii, 2680 Woodlawn Drive, Honolulu, HI, 96822, USA*
[5] *University Observatory Munich, Scheinerstr. 1, D-81679, Munich, Germany*
[6] *Dipartimento di Fisica e Astronomia, Universitá degli Studi di Bologna, Viale Berti Pichat 6/2, I-40127 Bologna, Italy*
[7] *Max-Planck Institute for Astronomy, D-69117, Heidelberg, Germany*

ABSTRACT

We have obtained *K*-band Multi-Object Spectrograph (KMOS) near-IR spectroscopy for 14 red supergiant stars (RSGs) in the young massive star cluster NGC 2100 in the Large Magellanic Cloud (LMC). Stellar parameters including metallicity are estimated using the *J*-band analysis technique, which has been rigorously tested in the Local Universe. We find an average metallicity for NGC 2100 of [Z] = -0.39 ± 0.10 *dex*, in good agreement with estimates from the literature for the LMC. Comparing our results in NGC 2100 with those for a Galactic cluster (at Solar-like metallicity) with a similar mass and age we find no significant change in the location of RSGs in the HR diagram. We combine the observed KMOS spectra to form a simulated integrated cluster spectrum and show that this is consistent with the average properties of the cluster.

Radial velocities are estimated for the targets and the dynamical properties are estimated for the first time within this cluster. The line-of-sight velocity dispersion is shown to be flat and is estimated to be $\sigma_{1D} = 3.4 \pm 0.4$ km s^{-1} with, however, a significant contribution from measurement errors. An upper limit on the dynamical mass of the cluster is derived as $M_{dyn} = (11.6 \pm 3.3) \times 10^4 M_\odot$ assuming virial equilibrium. Comparing this with the mass estimated using photometry we find the dynamical mass is larger owing to the contribution of measurement errors on the line-of-sight velocity dispersion.

Key words: stars: abundance, (stars:) supergiants, (galaxies:) Magellanic Clouds, galaxies: star clusters: individual: NGC 2100

1 INTRODUCTION

Young massive clusters (YMCs[1]) are important probes of the early evolution of star clusters and have increasingly been used as tracers of star formation in galaxies (e.g. Whitmore & Schweizer 1995; Miller et al. 1997; Zepf et al. 1999). Known to contain large populations of massive stars, YMCs are also important tracers of massive star formation, which is heavily clustered (de Wit et al. 2005; Parker & Goodwin 2007). In addition to being the birthplace of most of the massive stars in the Local Universe (> 20 M$_\odot$ stars in R136; Crowther et al. 2010), owing to the density of stars, YMCs are also the birthplace of rich stellar exotica found in the old population of globular clusters (Portegies Zwart et al. 2010, GCs).

Investigating the link between YMCs and older GCs is an important, uncertain, factor in the evolution of young clusters. As most stellar systems dissolve shortly after formation (Lada & Lada 2003), determining for how long bound systems can remain so is an important question to answer. Studying the dynamical properties of YMCs is, therefore, an

⋆ E-mail: lrp@roe.ac.uk

---

[1] A YMC is defined as < 100 Myr and > 10^4 M$_\odot$ (Portegies Zwart et al. 2010).

important tool to evaluate the likelihood that young clusters will survive.

Recently, the idea that globular clusters are simple stellar populations has been called into question based on chemical anomalies of light elements (C, N, O, Na and Al; e.g. Gratton et al. 2012). These anomalies are considered by most authors to be the signature of multiple stellar populations within globular clusters. Studying YMCs could therefore potentially help to constrain some of the proposed models for creating multiple stellar populations within GCs (e.g. Cabrera-Ziri et al. 2014). In addition, the study of YMCs in different environments can help bridge the gap between the understanding of star formation in the Solar-neighbourhood and that in the high–redshift Universe.

Over the last few years, medium resolution ($R \geqslant 3000$) near-IR spectroscopy has been shown to be a powerful tool to estimate stellar parameters for red supergiant stars (RSGs; Davies et al. 2010). RSGs are the final evolutionary stage of a massive star and, owing to their cool atmospheres ($T_{\mathrm{eff}} \sim 4000$; Davies, B., et al. 2013), are brightest at $\sim 1.1\,\mu m$. In star-forming galaxies, RSGs are the most luminous near-IR sources, therefore, by exploiting these wavelengths they can be observed out to large distances. Given that dust extinction is intrinsically lower at near-IR wavelengths and that the next generation of ground-/space-based telescopes will be optimised for observations at these wavelengths, RSGs are likely to become increasingly attractive targets by which to study distant star-forming galaxies.

The J-band analysis technique for estimating metallicities and stellar parameters of RSGs has been rigorously tested by Gazak et al. (2014a) and Davies et al. (2015). These authors show that metallicities can be estimated in extragalactic systems to a high level of accuracy and to a precision of $< 0.15\,dex$.

The availability of the K-band multi-object spectrograph (KMOS; Sharples et al. 2013) at the Very Large Telescope (VLT), has presented new opportunities for efficient observations of samples of RSGs in external galaxies to study their distribution and build-up of metals. Patrick et al. (2015) used KMOS observations to investigate the present-day metallicity of NGC 6822 ($d = 0.5\,\mathrm{Mpc}$) and Gazak et al. (2015) determined the metallicity gradient of NGC 300, a grand design spiral galaxy outside the Local Group ($d = 1.9\,\mathrm{Mpc}$), finding striking agreement with previous measurements from stars and H II regions.

In addition, Gazak et al. (2013) demonstrated that, after the appearance of the first RSGs within a YMC, the overall near-IR flux from the cluster is dominated by the RSGs ($\mathrm{F}_{J,RSG}/\mathrm{F}_J > 0.90$). Using this result, these authors showed that the spectrum from an unresolved star cluster can be used to estimate the average properties of the RSG population of the cluster using exactly the same analysis method as for single stars. Lardo et al. (2015) demonstrated this with KMOS spectroscopy of three unresolved YMCs in NGC 4038 in the Antennae ($d = 20\,\mathrm{Mpc}$), at Solar-like metallicity, finding good agreement with previous studies. With a multi-object spectrograph operating on the European Extremely Large Telescope, this technique could be used to measure metallicities of individual RSGs at distances of $> 10\,\mathrm{Mpc}$ and from YMCs out to potentially $> 100\,\mathrm{Mpc}$ (Evans 2011).

NGC 2100 is a YMC in the Large Magellanic Cloud (LMC), located near the large star-forming 30 Doradus region. With an age of $\sim 20\,\mathrm{Myr}$ (Elson 1991; Niederhofer et al. 2015), and a photometric mass of $4.6 \times 10^4 M_\odot$ (McLaughlin & van der Marel 2005, assuming King (1966) profiles), NGC 2100 falls within the mass and age range where the near-IR cluster light is dominated by RSGs (Gazak et al. 2013). This is supported by the large number of RSGs identified within this cluster (see Figure 1).

NGC 2100 is not a cluster in isolation. It is located in one of the most actively star-forming regions within the Local Group of galaxies. At $\sim 20\,\mathrm{Myr}$ old, the most massive members of this star cluster will have already exploded as supernovae. This should have had a profound effect on the surrounding gas and dust, and has potentially shaped the surrounding LMC 2 supershell (see Points et al. 1999).

In this study we estimate stellar parameters from KMOS spectroscopy for 14 RSGs which appear to be associated with NGC 2100. Section 2 describes the observations and data reduction, and in Section 3 we detail our results, focusing on radial velocities of the target stars where we derive the line-of-sight velocity dispersion, the dynamical mass of NGC 2100 and stellar parameters. Our results are discussed in Section 4 and conclusions are presented in Section 5.

2   OBSERVATIONS AND DATA REDUCTION

These observations were obtained as part of the KMOS Guaranteed Time Observations (PI: Evans 095.B-0022) in March 2015. The observations consisted of $8 \times 10\,\mathrm{s}$ exposures (seeing conditions $\sim 1''0$) taken with the YJ grating with sky offset exposures (S) interleaved between the object exposures (O) in an O, S, O observing pattern. In addition, a standard set of KMOS calibration frames were obtained as well as observations of HD 51506 (B5) as the telluric standard star. Figure 1 shows the observed RSGs overlaid on a J-band VISTA image of the surrounding region (Cioni et al. 2011).

The standard KMOS/esorex routines (SPARK; Davies, R. I., et al. 2013) were used to calibrate and reconstruct the data cubes. Telluric correction was performed using the 24-arm telluric-correction routine using the methodology described in detail by Patrick et al. (2015). Briefly, corrections are made to the standard telluric recipe to account for slight differences in wavelength calibration between the telluric and science spectra. This is implemented using an iterative cross-correlation approach. Additionally, differences in the strength of the telluric features are corrected by applying a simple scaling using the equation:

$$T_2 = (T_1 + c)/(1 + c) \qquad (1)$$

where T_2 is the scaled telluric-standard spectrum, T_1 is the uncorrected telluric-standard spectrum and c is the scaling parameter which is varied from $c = -0.5$ to $c = 0.5$ in increments of 0.02. The best-fit value is chosen based on the overall standard deviation of the spectrum, i.e. the c value producing the smallest σ is selected. Once these corrections are accounted for, the science spectra are divided by the appropriate telluric spectrum for that particular KMOS integral field unit (IFU).

Table 1. Observed properties of VLT-KMOS targets in NGC 2100

ID	S/N	J^a	H^a	$K_s{}^a$	RV (km s^{-1})	Notes[b]
J054147.86-691205.9	320	9.525	8.603	8.200	250.3 ± 4.7	D15
J054152.51-691230.8	200	10.413	9.526	9.155	249.3 ± 2.6	D16
J054157.44-691218.1	200	9.811	9.036	8.738	245.6 ± 3.5	C2
J054200.74-691137.0	260	9.900	9.017	8.683	248.8 ± 2.7	C8
J054203.90-691307.4	250	9.839	8.996	8.740	251.1 ± 2.8	B4
J054204.78-691058.8	210	10.319	9.427	9.159	256.1 ± 4.0	. . .
J054206.36-691220.2	200	10.371	9.480	9.159	255.7 ± 4.9	B17
J054206.77-691231.1	250	9.977	9.150	8.807	250.6 ± 3.4	A127
J054207.45-691143.8	200	10.482	9.610	9.351	252.5 ± 3.0	C12
J054209.66-691311.2	240	9.976	9.136	8.841	254.3 ± 4.1	B47
J054209.98-691328.8	250	10.021	9.150	8.823	250.2 ± 3.0	C32
J054211.56-691248.7	300	9.557	8.617	8.264	255.5 ± 4.3	B40
J054211.61-691309.2	150	10.943	10.090	9.788	256.6 ± 6.1	B46
J054212.20-691213.3	200	10.440	9.622	9.335	260.0 ± 4.8	B22

[a] Photometric data from 2MASS, with typical errors on J, H, and K_s of 0.024, 0.026 and 0.022 mag respectively.
[b] Cross-identifications in final column from Robertson (1974).
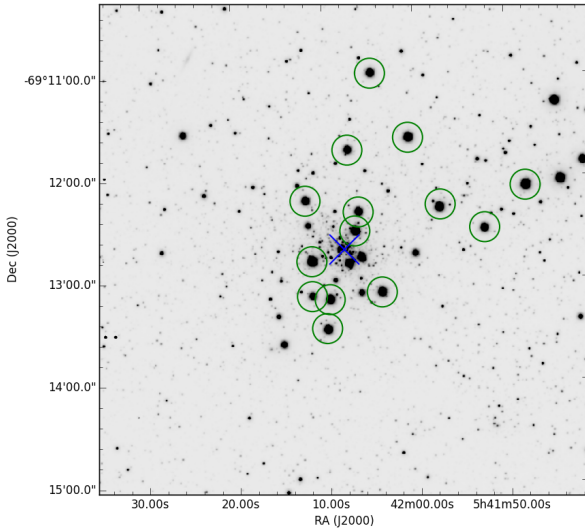

Figure 1. Positions of the KMOS targets in NGC 2100 overlaid on a VISTA J-band image (Cioni et al. 2011). Green circles indicate KMOS targets. The adopted cluster centre has been marked by a blue cross.

3 RESULTS

3.1 Radial velocities

Radial velocities are estimated using an iterative cross-correlation method. To ensure systematic shifts are removed, the observed spectra are first cross-correlated against a spectrum of the Earth's atmosphere, taken from the European Southern Observatory web pages[2], at a much higher spectral resolution than that of KMOS. This spectrum is then degraded to the resolution of the observations using a simple Gaussian filter. The cross-correlation is performed within the 1.140–1.155 μm region, as a strong set of reliable telluric features dominates this region, with minimal contamination from stellar features. The shift arising from this region is typ-

ically 0–10 km s^{-1} and is then applied to the ⬚–1.22 μm region, i.e. where the radial velocity is estimated.

Once the observed spectra are on a consistent wavelength solution, an initial estimate of the radial velocity is obtained by cross-correlating the science spectra with an appropriate synthetic RSG spectrum in the 1.16–1.22 μm region. This wavelength region is selected based on the dominance of atomic features in RSG spectra at these wavelengths. To increase reliability, this initial estimate is improved upon by using seven strong stellar absorption lines which are chosen based on line strength and the lack of significant telluric contamination.

Radial velocities are independently calculated for each line using, again, the iterative cross-correlation method. This results in seven estimates of the radial velocity for each star, which are then compared. Any line that results in a radial velocity that is an obvious outlier to the distribution is rejected (i.e. several 10 km s^{-1} discrepant from any other value). This can occasionally be the case when the cross-correlation incorrectly centres on a different spectral line; a simple visual inspection of the resulting spectra, once the shift has been implemented, is sufficient to remove these rare cases.

The final radial velocity for each star is the mean of the estimates from the (non-rejected) lines, where the error on this mean is calculated by taking the standard deviation of the data, normalised by the number of regions used ($err = \sigma/N_{regions}$). This method is known to work well for KMOS spectra (Lapenna et al. 2015; Patrick et al. 2015).

Figure 2 shows our stellar radial velocity estimates as a function of distance from the centre of the cluster, compared with the systemic radial velocity of the LMC (green dashed line). Given the low dispersion of the radial velocity measurements for the KMOS targets, we confirm that all of the target RSGs within this sample have velocities consistent with membership of NGC 2100. The average radial velocity of the sample is 251.8 ± 4 km s^{-1}. This value is in reasonable agreement with previous measurements for two OB-type stars in the cluster (Evans et al. 2015) as well as the
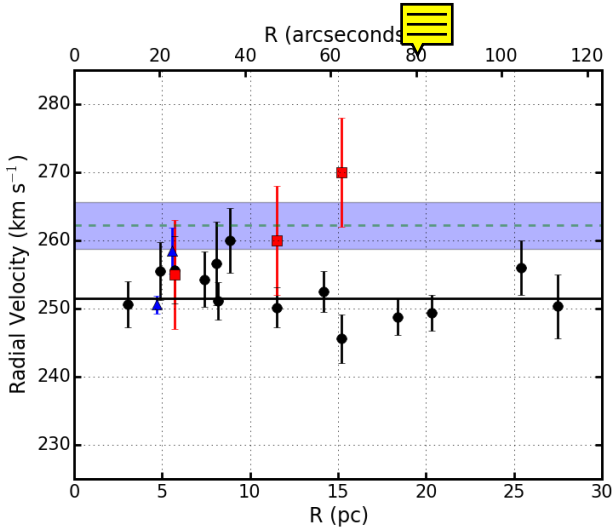
Figure 2. Radial velocities of KMOS targets shown as a function of distance from the cluster centre. The green dashed line shows the LMC systemic velocity with the uncertainty highlighted by the blue shaded region ($262.2 \pm 3.4\,\mathrm{km\,s^{-1}}$; McConnachie 2012). The solid black line shows the mean of the sample ($251.5 \pm 3.4\,\mathrm{km\,s^{-1}}$). The blue triangles show estimates for two OB-type stars (Evans et al. 2015) and the red squares show previous estimates for three of our targets (Jasniewicz & Thevenin 1994).

results from four RSGs in NGC 2100 (Jasniewicz & Thevenin 1994, henceforth JT94; three of which were observed in the current study). Table 2 contains the details of previous radial velocity measurements within NGC 2100. We conclude that there exists no significant difference between our measurements and previous estimates within NGC 2100. This is an additional confirmation that absolute radial velocities can be precisely measured with KMOS spectra.

3.2   Velocity dispersion

An upper limit to the line-of-sight velocity dispersion (σ_{1D}) is calculated using the equations:

$$\mu = \frac{1}{\sum_i 1/\sigma_i^2} \sum_i \frac{RV_i}{\sigma_i} \tag{2}$$

$$Var = \frac{1}{\sum_i 1/\sigma_i^2} \sum_i \frac{(RV_i - \mu)^2}{\sigma_i^2} \tag{3}$$

$$\sigma_{1D} = \sqrt{Var \frac{N}{N-1}} \tag{4}$$

where σ_i is the uncertainty on the radial velocity measurement RV_i, μ is the weighted mean and N is the number of stars in the sample. Figure 3 shows the average line-of-sight velocity dispersion as a function of radius for RSGs in NGC 2100, where σ_{1D} is calculated for each star using all stars closer to the cluster centre than the star in question. The uncertainties indicated in this figure are defined as the standard deviation of the radial velocities within the given distance, normalised by the number of measurements in the sample. We see that the dispersion is consistent with a flat profile with an average of $3.4 \pm 0.4\,\mathrm{km\,s^{-1}}$. The scatter
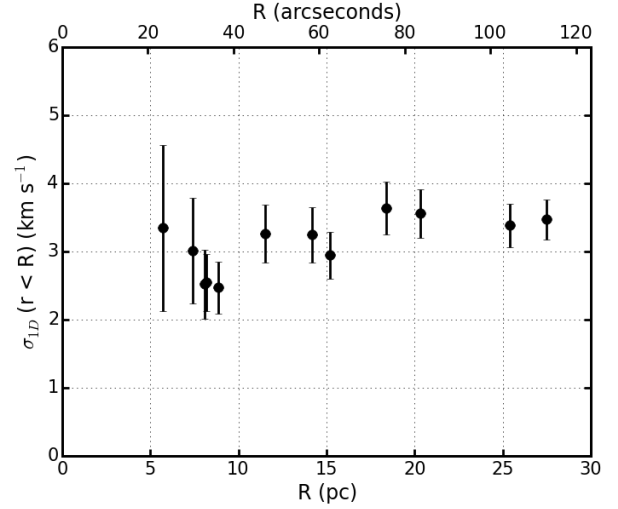

Figure 3. Observed line-of-sight velocity dispersion as a function of the distance from the centre of NGC 2100. The measurement of σ_{1D} includes the radial velocities of all RSGs internal to the target in question. The average σ_{1D} from this figure is $3.4 \pm 0.4\,\mathrm{km\,s^{-1}}$.

within 10 pc could, as a result of the low number statistics at small radii. A discussion on how binarity affects this distribution is given in Section 4.

To estimate the contribution of measurement errors we performed a simple Monte Carlo simulation. For each radial velocity estimate, we drew random samples from a normal distribution centred on zero with a standard deviation matching that of the error on the estimated radial velocity. Using this data set, the average line-of-sight velocity dispersion was computed for the whole sample (as we found no evidence for variations in σ_{1D}). This procedure was then repeated 10 000 times and the resulting distribution is shown in Figure 4. From this figure, we can see that the contribution of the measurement errors can completely account for the measured σ_{1D} of the cluster. Therefore, using the data available, we conclude that we can only place an upper limit on the line-of-sight velocity dispersion of $\sigma_{1D} = 3.4 \pm 0.4\,\mathrm{km\,s^{-1}}$ for NGC 2100.

3.3   Dynamical mass

Using σ_{1D} as an upper limit on the velocity distribution, one can calculate an upper limit on dynamical mass of the cluster using the virial equation:

$$M_{dyn} = \frac{\eta \sigma_{1D}^2 r_{eff}}{G} \tag{5}$$

where M_{dyn} is the dynamical mass and $\eta = 6r_{vir}/r_{eff} = 9.75$ – providing the density profile of the cluster is sufficiently steep (Portegies Zwart et al. 2010) – where $r_{eff} = 4.41\,\mathrm{pc}$ for NGC 2100 (McLaughlin & van der Marel 2005). However, NGC 2100 has a relatively shallow density profile ($\gamma = 2.44 \pm 0.14$; Mackey & Gilmore 2003) which means $\eta < 9.75$. Using $\sigma_{1D} = 3.4 \pm 0.4\,\mathrm{km\,s^{-1}}$ and equation 5, the dynamical mass of NGC 2100 is $M_{dyn} = (8.1 \pm 3.3) \times 10^4 M_\odot$. Comparing this to the photometric mass $M_{phot} = (2.3 \pm 1.0) \times 10^4 M_\odot$ (McLaughlin & van der Marel 2005), we see that the

Table 2. Literature stellar radial velocity measurements within NGC 2100

	ID		RV (km s^{-1})		Reference	Notes
Lit.	current study	Lit.	current study			
AAΩ 30 Dor 407	—	258.5 ± 3.4	...	Evans et al. (2015)	O9.5 II
AAΩ 30 Dor 408	—	250.6 ± 1.3	...	Evans et al. (2015)	B3 Ia
R74 B17	J054206.36-691220.2	255 ± 8	255.7 ± 4.9	Jasniewicz & Thevenin (1994)	
R74 C2	J054157.44-691218.1	270 ± 8	245.6 ± 3.5	Jasniewicz & Thevenin (1994)	
R74 C32	J054209.98-691328.8	260 ± 8	250.2 ± 3.0	Jasniewicz & Thevenin (1994)	
R74 C34	—	265 ± 8	...	Jasniewicz & Thevenin (1994)	

ID and RV columns: the first value is from the literature and the second is from the current study.
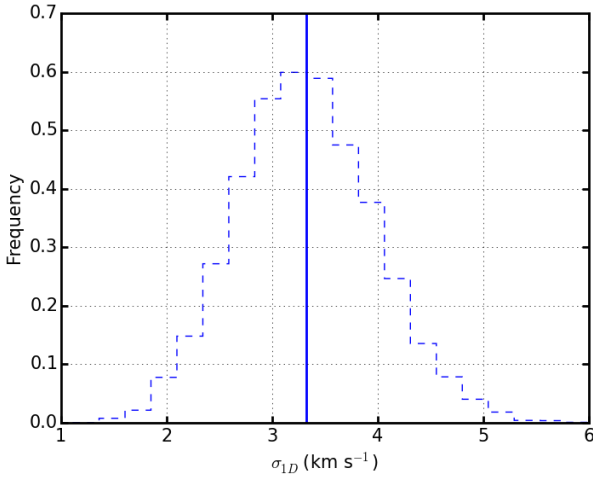

Figure 4. Histogram of results for 10 000 realisations of the simulated line-of-sight velocity dispersion of NGC 2100 to measure the contribution of measurement errors. The blue line shows the mean value for the distribution at 3.3 ± 0.7 km s^{-1}, which is the adopted value for the contribution of measurement errors for our sample.

dynamical mass is significantly larger. Gieles et al. (2010) explain this discrepancy by demonstrating that binary motions can increase the measured velocity dispersion profile. Demonstrating this, Hénault-Brunet et al. (2012) noted that, had binarity been neglected, they would have measured a σ_{1D} a factor of five higher for R136 (a YMC in the LMC). However, the mean lifetime for RSGs within binary systems is significantly decreased and, where mass transfer occurs, the number of RSGs drastically decreases (Eldridge et al. 2008). We can therefore expect that the number of RSGs in close binary systems is very small (Davies et al. 2009). The fraction of RSGs in longer period binary systems is more uncertain; however, these systems would increase the line-of-sight velocity dispersion to a lesser degree.

The above argument would lead one to the conclusion that the measured σ_{1D} is not increased owing to binary motions, as our sample is expected to be entirely single objects and therefore the difference between the mass estimates must be the result of an alternative explanation. However, while these assumptions hold, the true dispersion appears to be unresolved, the difference between the dynamical and photometric mass estimates can be accounted for when one considers that the true dispersion is likely to be significantly smaller than the contribution of our measurement errors.

3.4 Stellar parameters

Stellar parameters are estimated for each target using the *J*-band analysis technique described initially by Davies et al. (2010) and tested rigorously by Gazak et al. (2014a) and Davies et al. (2015). These studies show that by using a narrow spectral window within the *J*-band one can accurately derive overall metallicities ([Z]) to better than $\pm 0.15 \, dex$ at the resolution of KMOS observations with S/N $\geqslant$ 100. Patrick et al. (2015) built on this by demonstrating the feasibility of this technique using KMOS spectra.

The analysis uses synthetic RSG spectra, extracted from MARCS model atmospheres (Gustafsson et al. 2008), computed with corrections for non-local thermodynamic equilibrium for lines from titanium, iron, silicon and magnesium (Bergemann et al. 2012, 2013, 2015). The parameter ranges for the grid of synthetic RSG spectra are listed in Table 3. The synthetic spectra are compared with observations using a χ-squared minimisation approach where the synthetic spectra are degraded to the resolution and sampling of the observations.

Estimated stellar parameters are listed in Table 4. Reliable parameters could not be estimated for one star within the sample (J054211.61-691309.2). This star is rejected from further analysis, pending a more rigorous investigation into why reliable parameters could not be estimated. An initial investigation reveals that this star has sufficient S/N (see Table 1), displays no obvious residuals from the reduction process and is not an obvious blend in the KMOS image. Figure 5 shows the observed KMOS spectra (black) compared to their best-fitting models (red). The average metallicity for the 13 stars with good fits is [Z] = $-0.39 \pm 0.10 \, dex$.

The average metallicity in NGC 2100 estimated here is in good agreement with estimates of the cluster metallicity using isochrone fitting to the optical colour-magnitude diagram ($-0.4 \, dex$; Niederhofer et al. 2015). The only other estimate of stellar metallicity within this cluster is from JT94 who estimated metallicities using optical spectroscopy of four RSGs. These authors found an average metallicity for NGC 2100 of [Fe/H] = $-0.32 \pm 0.03 \, dex$, which is in good agreement with our estimate. We find that there are three targets in common with our study: B17, C2 and C32 (using the Robertson 1974, nomenclature). Comparing results we find B17 (J054206.36-691220.2) is the target that does not have reliable stellar parameters.

The results for C2 (J054157.44-691218.1) are consistent with what is reported in JT94, although we note that the surface gravity reported here agrees with the estimated photometric surface gravity, and the spectroscopic surface grav-
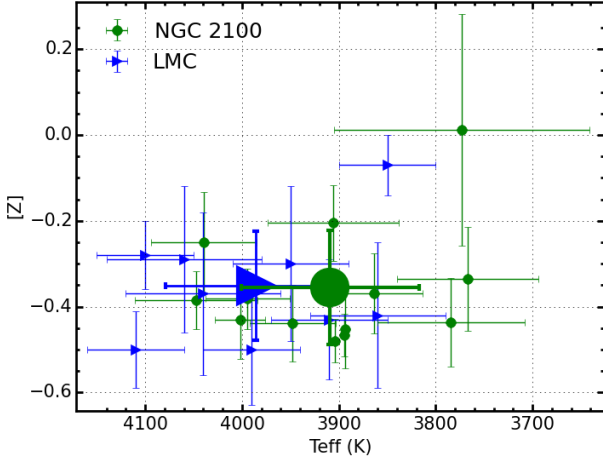
Figure 6. Estimated metallicities for NGC 2100 RSGs in this study shown against effective temperature (green dots). For comparison we show the distribution of LMC RSGs from Davies et al. (2015, blue triangles) with good agreement between the means of the two samples.

Table 3. Model grid used for the spectroscopic analysis.

Model Parameter	Min.	Max.	Step size
T_{eff} (K)	3400	4400	100
[Z] (dex)	−1.0	1.0	0.1
$\log g$ (cgs)	−1.00	1.00	0.25
ξ (km s^{-1})	1.0	5.0	0.2

ity in JT94 is significantly lower. In addition, we note that the microturbulence value quoted in the current study is on the edge of the allowed model grid. The results for C32 (J054209.98-691328.8) are consistent with what is reported in JT94, although we note that the best fit microturbulence value is also at the edge of the model grid.

Using the same analysis technique as in this study, Davies et al. (2015) estimate metallicities for nine RSGs within the LMC, finding an average value of -0.37 ± 0.14 *dex*, which our estimate agrees well with. In Figure 6, we compare the effective temperatures and metallicities from NGC 2100 with those estimated for RSGs elsewhere in the LMC. We find good agreement in the distribution of temperatures from the two studies, with the average agreeing well. The range in [Z] from the LMC population is slightly larger than that of the NGC 2100 RSGs, which is expected when comparing a star cluster with an entire galaxy; however, the average for the two studies agree very well.

4 DISCUSSION

4.1 Stellar parameters

Luminosities have been estimated for our sample using the bolometric correction from Davies, B., et al. (2013) and a H–R diagram for the cluster is presented in Figure 7. Overlaid on this H–R diagram are SYCLIST stellar isochrones for SMC-
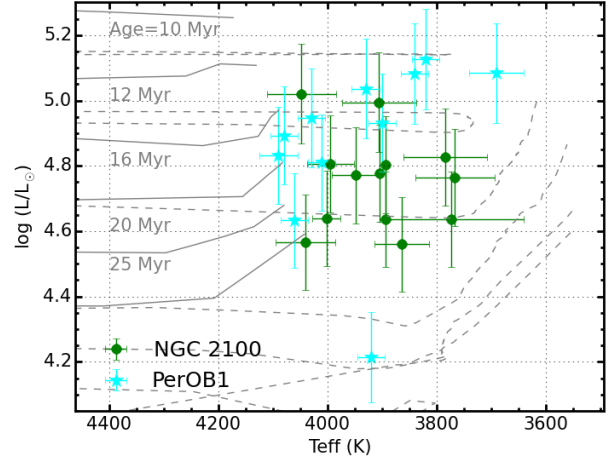

Figure 7. H–R diagram for 12 RSGs in NGC 2100. Isochrones for solar (dashed lines; Ekström et al. 2012) and SMC-like (solid lines; Georgy et al. 2013) metal abundances, in which stellar rotation is 40% of the break-up velocity, are shown for ages of 10-32 Myr. For comparison, 11 RSGs from the Galactic YMC Perseus OB-1 are overlaid (Gazak et al. 2014a). The best-fit isochrone to the observed data has an age of 20 ± 5 Myr for both SMC- and solar-like metallicities.

like (solid lines; Georgy et al. 2013) and Solar-like (dashed lines; Ekström et al. 2012) models, where stellar rotation is 40% of break-up velocity. Even though the temperatures covered by the SMC-like models do not represent the distribution of temperatures observed in this study, they remain useful to constrain the age of NGC 2100. The Solar-like models (dashed) demonstrate that, when compared with the SMC-like models, increasing the metallicity of the sample (a) decreases the average temperature of the RSGs (something which is not observed by Patrick et al. 2015), (b) induces so called 'blue loop' behaviour for the youngest models and (c) decreases the luminosity for the youngest models.

In addition, results for 11 RSGs from the Galactic star cluster Perseus OB-1 (PerOB1; Gazak et al. 2014b) are overlaid in Figure 7 (blue stars) for which stellar parameters were estimated using the same analysis technique as in this study. PerOB1 is a cluster with a similar mass and age (2×10^4 M$_\odot$ and 14 Myr respectively; Currie et al. 2010) as NGC 2100, and a comparison between the stellar components of these two clusters using a consistent analysis technique is useful to highlight differences in stellar evolution within clusters at different metallicities.

We can see from Figure 7 that, generally, the estimated temperatures are in good agreement between the two clusters. The median luminosity for the PerOB1 targets ($10^{4.93}$ L$_\odot$) is slightly above that of NGC 2100 ($10^{4.77 \pm 0.15}$ L$_\odot$) which could represent the slight difference in the ages of the two clusters. As PerOB1 is younger, the average mass for a RSG in the cluster will be larger than the average in NGC 2100. Therefore, we would expect to see higher luminosity RSGs in PerOB1. However, the difference between the two samples is barely significant and is consistent with a constant luminosity. The average effective temperatures for the two data sets (NGC 2100: 3910 ± 15 K, PerOB1: 3940 ± 10 K) are in reasonable agreement, where
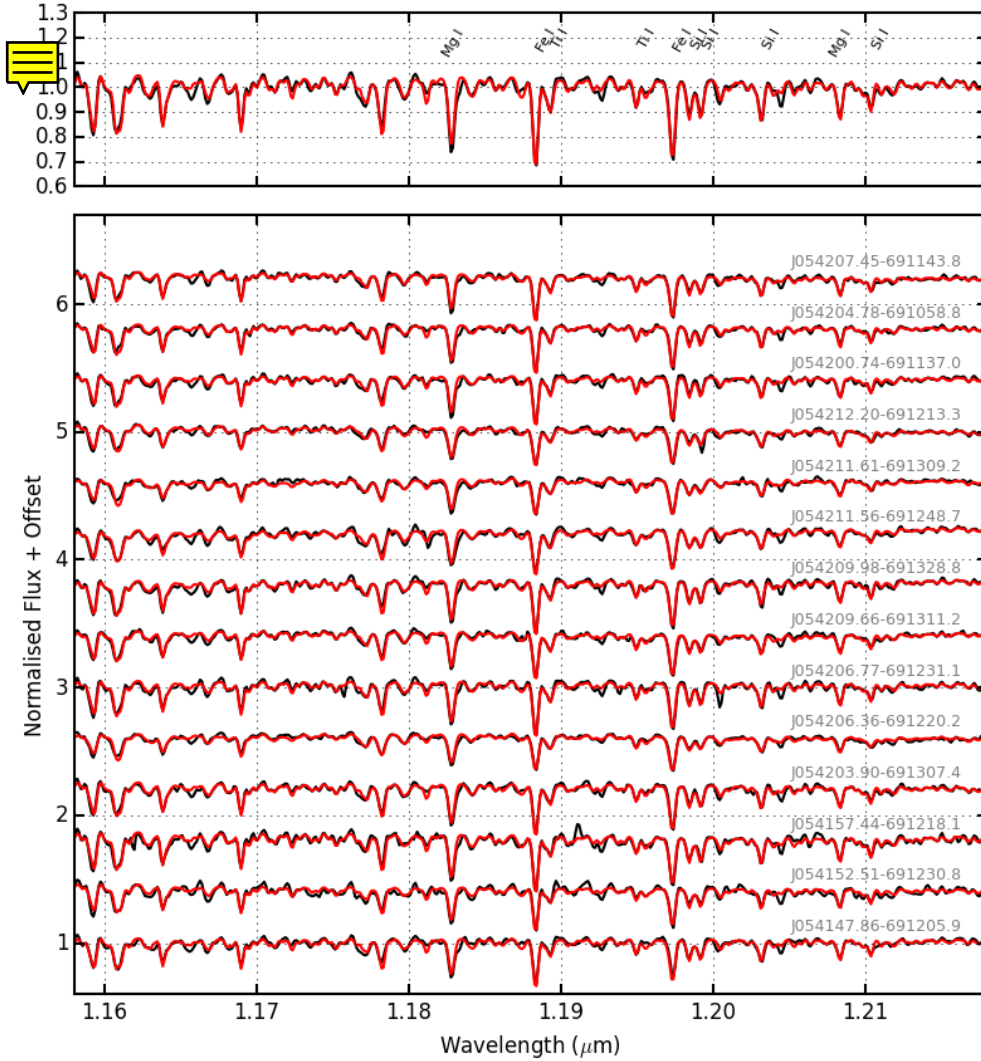
Figure 5. KMOS spectra of RSGs in NGC 2100 and their associated best-fit models (black and red lines respectively). Top panel shows the simulated integrated-light cluster spectrum. Bottom panel shows spectra for the individual RSGs. The lines used for the analysis from left-to-right by species are Fe I $\lambda\lambda 1.188285, 1.197305$; Mg I $\lambda\lambda 1.182819, 1.208335$; Si I $\lambda\lambda 1.198419, 1.199157, 1.203151, 1.210353$; Ti I $\lambda\lambda 1.189289, 1.194954$.

the spread in temperatures is slightly larger for PerOB1 ($\sigma_{PerOB1} = 120$ K, $\sigma_{GC\,2100} = $ particularly so for the highest luminosity targets within the PerOB1 sample. Overall, by comparing these two star clusters with a similar mass, age and stellar population, we conclude that there exists no significant difference in appearance on the –R diagram of RSGs within star clusters of different metallicities.

4.2 Velocity dispersion and dynamical mass

This study represents the first estimate of an upper limit to the line-of-sight velocity dispersion profile for NGC 2100. Comparing this estimate with that of other YMCs in the Local Universe is useful to ascertain if this cluster shares similar properties with other YMCs. We find the dynamical properties NGC 2100 are well matched by other clusters with similar masses and ages, particularly so with RSGC01, a Galactic YMC (Davies et al. 2007).

Owing to the non-negligible contribution from measurement errors, the σ_{1D} adopted here is an upper limit to the true dispersion within the cluster which is likely to be significantly smaller than the contribution of the measurement errors. Using the data available, we can rule out an σ_{1D} value significantly larger than $3.4 \pm 0.4 \,\mathrm{km\,s^{-1}}$, however, the dispersion we measure is consistent with zero dispersion within the cluster.

By extension, the dynamical mass estimated here is therefore also an upper limit to the true mass of the cluster. There are several factors that could alter the value of the dynamical mass estimate. The likely value of the η parameter is discussed in Section 3.3 and any change in this value will act to decrease the estimated dynamical mass. Using a lower limit of η does not account for the discrepancy between the dynamical mass measured here and the literature photometric mass of the cluster. A reduction in the line-of-sight

Table 4. Physical parameters determined for the KMOS targets in NGC 2100

Target	IFU	ξ (km s^{-1})	[Z]	$\log g$	T$_{eff}$ (K)	Notes[a]
J054147.86−691205.9	7	3.6 ± 0.19	-0.39 ± 0.07	0.12 ± 0.12	4050 ± 65	D15
J054152.51−691230.8	9	3.5 ± 0.18	-0.43 ± 0.09	0.42 ± 0.18	4000 ± 25	D16
J054157.44−691218.1	6	5.0 ± 0.10	-0.38 ± 0.07	0.18 ± 0.13	3990 ± 45	C2
J054200.74−691137.0	4	4.2 ± 0.23	-0.44 ± 0.10	0.17 ± 0.10	3780 ± 75	C8
J054203.90−691307.4	12	4.6 ± 0.14	-0.47 ± 0.05	0.24 ± 0.13	3890 ± 50	B4
J054204.78−691058.8	3	4.1 ± 0.20	-0.45 ± 0.09	0.48 ± 0.10	3890 ± 50	. . .
J054206.36−691220.2	24	2.5 ± 0.47	0.01 ± 0.27	0.45 ± 0.11	3770 ± 130	B17
J054206.77−691231.1	10	5.0 ± 0.10	-0.48 ± 0.05	0.24 ± 0.13	3900 ± 50	A127
J054207.45−691143.8	2	4.0 ± 0.21	-0.37 ± 0.09	0.48 ± 0.13	3860 ± 50	C12
J054209.66−691311.2	14	3.7 ± 0.20	-0.34 ± 0.12	0.06 ± 0.21	3770 ± 75	B47
J054209.98−691328.8	11	5.0 ± 0.10	-0.44 ± 0.09	0.16 ± 0.20	3950 ± 45	C32
J054211.56−691248.7	20	3.8 ± 0.19	-0.21 ± 0.09	-0.01 ± 0.17	3910 ± 70	B40
J054211.61−691309.2	18	2.1 ± 0.24	0.34 ± 0.08	0.75 ± 0.13	3800 ± 50	B46
J054212.20−691213.3	22	3.3 ± 0.21	-0.25 ± 0.12	0.36 ± 0.25	4040 ± 55	B22
NGC 2100 average[b]		4.0 ± 0.1	-0.36 ± 0.03	0.26 ± 0.04	3910 ± 15	

[a] ID in final column from Robertson (1974).
[b] Average values neglecting J054211.61−691309.2 owing to the spurious metallicity measurement, where the error reported represents the errors on the respective means rather than the standard deviation of the samples.

velocity by $\sim 25\%$ is sufficient to account for the differences between the mass estimates.

4.3 Simulated cluster spectrum analysis

We can use the individual stars in NGC 2100 to simulate the analysis of a YMC in the more distant Universe, using the assumption that RSGs dominate the near-IR flux from such a cluster (Gazak et al. 2013). Gazak et al. (2014a) use this assumption to create a simulated integrated-light cluster spectrum for PerOB1 and show that, by analysing the combined spectrum from their 11 RSGs, the resulting parameters are consistent with the average parameters estimated using the individual stars. NGC 2100 has a similar mass and age to PerOB1 and Gazak et al. (2014a) study a similar number of RSGs to this study, therefore, a direct comparison between the two clusters is useful to investigate potential metallicity dependencies.

To create a simulated integrated-light cluster spectrum we sum all the individual RSG spectra weighted by their J-band luminosities. The resulting spectrum is then degraded to the lowest resolution spectrum of the sample using a simple Gaussian filter. The top panel of Figure 5 shows the resulting integrated-light cluster spectrum. This spectrum is then analysed in the same way described in Section 3.4 for a single RSG. The results of this analysis are what one would expect from KMOS observations of more distant YMCs where individual stars cannot be resolved. We find a metallicity of $-0.32 \pm 0.11\,dex$, an effective temperature of 3953 ± 49 K, a surface gravity of $0.34 \pm 0.23\,dex$ and a microturbulent velocity of 3.8 ± 0.2 km s^{-1} which agree well with the average of the individual RSG parameters.

5 CONCLUSIONS

Using KMOS spectra of 14 RSGs in NGC 2100 we have for the first time estimated the dynamical properties of this YMC. Radial velocities have been estimated using KMOS, to a precision of < 5 km s^{-1}, demonstrating that this in-

strument can be used to study the dynamical properties of star clusters in external galaxies.

An upper limit to the average line-of-sight velocity dispersion of $\sigma_{1D} = 3.4 \pm 0.4$ km s^{-1} has been estimated and we find no evidence for spatial variations. We compare the line-of-sight velocity dispersion estimated here with that of other YMCs in the Local Universe and find that NGC 2100 agrees well with other massive clusters. Using the average velocity dispersion within NGC 2100 allows an upper limit on the dynamical mass to be calculated (assuming virial equilibrium) as $M_{dyn} = (11.6 \pm 5.3) \times 10^4 M_\odot$. This value is shown to be larger than the literature photometric mass; however, we note that, as the true velocity dispersion is likely to be significantly smaller than our upper limit, this result is not significant.

In addition to estimating the dynamical properties of NGC 2100, we have also reliably estimated stellar parameters for 13 RSGs in NGC 2100 using the new J-band analysis technique (Davies et al. 2010). We find the average metallicity for RSGs in NGC 2100 is [Z] $= -0.36 \pm 0.03\,dex$, which agrees well with previous studies within this cluster and with studies of the young stellar population of the LMC.

The H–R diagram of NGC 2100 is compared with that of PerOB1: a Galactic YMC with a similar age, mass and stellar population. Using stellar parameters estimated from RSGs using the same analysis technique as that in this study, we demonstrate that there exists no significant difference in the appearance of the H–R diagram of YMCs between Solar- and LMC-like metallicities.

By combining the individual RSG spectra within NGC 2100, we have simulated an integrated-light cluster spectrum and proceeded to analyse this spectrum using the same techniques for that of the individual RSGs, as RSGs dominate the cluster light in the J-band (Gazak et al. 2013). The results of this technique demonstrate the potential of this analysis for integrated light spectra of more distant YMCs in low-metallicity environments. We find good agreement using the integrated-light cluster spectrum with the average results of the individual RSGs.

ACKNOWLEDGEMENTS

REFERENCES

Bergemann, M., Kudritzki, R.-P., Plez, B., et al. 2012, ApJ, 751, 156

Bergemann, M., Kudritzki, R.-P., Würl, M., et al. 2013, ApJ, 764, 115

Bergemann, M., Kudritzki, R.-P., Gazak, Z., Davies, B., & Plez, B. 2015, ApJ, 804, 113

Cabrera-Ziri, I., Bastian, N., Davies, B., et al. 2014, MNRAS, 441, 2754

Cioni, M.-R. L., Clementini, G., Girardi, L., et al. 2011, A&A, 527, A116

Crowther, P. A., Schnurr, O., Hirschi, R., et al. 2010, MNRAS, 408, 731

Currie, T., Hernandez, J., Irwin, J., et al. 2010, ApJS, 186, 191

Davies, B., Figer, D. F., Kudritzki, R.-P., et al. 2007, ApJ, 671, 781

Davies, B., Origlia, L., Kudritzki, R.-P., et al. 2009, ApJ, 696, 2014

Davies, B., Kudritzki, R.-P., & Figer, D. F. 2010, MNRAS, 407, 1203

Davies, B., Kudritzki, R.-P., Plez, B., et al. 2013, ApJ, 767, 3

Davies, B., Kudritzki, R.-P., Gazak, Z., et al. 2015, ApJ, 806, 21

Davies, R. I., Agudo Berbel, A., Wiezorrek, E., et al. 2013, A&A, 558, A56

de Wit, W. J., Testi, L., Palla, F., & Zinnecker, H. 2005, A&A, 437, 247

Ekström, S., Georgy, C., Eggenberger, P., et al. 2012, A&A, 537, A146

Eldridge, J. J., Izzard, R. G., & Tout, C. A. 2008, MNRAS, 384, 1109

Elson, R. A. W. 1991, ApJS, 76, 185

Evans, C. J., Davies, B., Kudritzki, R.-P., et al. 2011, A&A, 527, A50

Evans, C. J., van Loon, J. T., Hainich, R., & Bailey, M. 2015, A&A, 584, A5

Gazak, J. Z., Bastian, N., Kudritzki, R.-P., et al. 2013, MNRAS, 430, L35

Gazak, J. Z., Davies, B., Kudritzki, R., Bergemann, M., & Plez, B. 2014a, ApJ, 788, 58

Gazak, J. Z., Davies, B., Bastian, N., et al. 2014b, ApJ, 787, 142

Gazak, J. Z., Kudritzki, R., Evans, C., et al. 2015, ApJ, 805, 182

Georgy, C., Ekström, S., Eggenberger, P., et al. 2013, A&A, 558, A103

Gieles, M., Sana, H., & Portegies Zwart, S. F. 2010, MNRAS, 402, 1750

Gratton, R. G., Carretta, E., & Bragaglia, A. 2012, A&A Rev., 20, 50

Gustafsson, B., Edvardsson, B., Eriksson, K., et al. 2008, A&A, 486, 951

Hénault-Brunet, V., Evans, C. J., Sana, H., et al. 2012, A&A, 546, A73

Jasniewicz, G., & Thevenin, F. 1994, A&A, 282, 717

King, I. R. 1966, AJ, 71, 64

Lada, C. J., & Lada, E. A. 2003, ARA&A, 41, 57

Lapenna, E., Origlia, L., Mucciarelli, A., et al. 2015, ApJ, 798, 23

Lardo, C., Davies, B., Kudritzki, R.-P., et al. 2015, ApJ, 812, 160

Mackey, A. D., & Gilmore, G. F. 2003, MNRAS, 338, 85

Massey, P., & Hunter, D. A. 1998, ApJ, 493, 180

McConnachie, A. W. 2012, AJ, 144, 4

McLaughlin, D. E., & van der Marel, R. P. 2005, ApJS, 161, 304

Miller, B. W., Whitmore, B. C., Schweizer, F., & Fall, S. M. 1997, AJ, 114, 2381

Niederhofer, F., Hilker, M., Bastian, N., & Silva-Villa, E. 2015, A&A, 575, A62

Parker, R. J., & Goodwin, S. P. 2007, MNRAS, 380, 1271

Patrick, L. R., Evans, C. J., Davies, B., et al. 2015, ApJ, 803, 14

Points, S. D., Chu, Y. H., Kim, S., et al. 1999, ApJ, 518, 298

Portegies Zwart, S. F., McMillan, S. L. W., & Gieles, M. 2010, ARA&A, 48, 431

Robertson, J. W. 1974, A&AS, 15, 261

Sharples, R., Bender, R., Agudo Berbel, A., et al. 2013, The Messenger, 151, 21

Whitmore, B. C., & Schweizer, F. 1995, AJ, 109, 960

Zepf, S. E., Ashman, K. M., English, J., Freeman, K. C., & Sharples, R. M. 1999, AJ, 118, 752